European Congress on Computational Methods in Applied Sciences and Engineering
ECCOMAS 2004
P. Neittaanmäki, T. Rossi, S. Korotov, E. Oñate, J. Périaux, and D. Knörzer (eds.)
Jyväskylä, 24–28 July 2004

HYBRID LES-RANS USING SYNTHESIZED TURBULENCE FOR FORCING AT THE INTERFACE

L. Davidson[⋆] and M. Billson[†]

[⋆,†]Division of Thermo and Fluid Dynamics, Department of Mechanical Engineering
Chalmers University of Technology, SE-412 96 G¨oteborg, Sweden
[⋆]e-mail: lada@tfd.chalmers.se, web page: http://www.tfd.chalmers.se/˜lada

[†]e-mail: billson@tfd.chalmers.se

Key words: LES, hybrid LES-RANS, DES, synthesized turbulence, forcing term, inlet boundary conditions, embedded LES.

Abstract. *The main bottle neck for using Large Eddy Simulations at high Reynolds number is the requirement of very fine meshes near walls. Hybrid LES-RANS was invented to get rid of this limitation. In this method unsteady RANS (URANS) is used near walls and away from walls LES is used. The matching between URANS and LES takes place in the inner log-region.*

In the present paper a method to improve standard LES-RANS is evaluated. The improvement consists of adding instantaneous turbulent fluctuations (forcing conditions) at the matching plane between the LES and URANS regions in order to provide the equations in the LES region with relevant turbulent structures. The turbulent fluctuations are taken from synthesized homogeneous turbulence assuming a modified von Kármán spectrum. Both isotropic and non-isotropic fluctuations are generated. The turbulent length scale $k^{3/2}/\varepsilon$ and the turbulent kinetic energy are used as input and they are taken from time-averaged DNS data at the location of the interface plane ($y^+ = 60$). The non-isotropic fluctuations are generated in the principal coordinate system of the DNS Reynolds stress tensor. They are then scaled to fit the DNS Reynolds tensor in the principal coordinate system. After that they are transformed back to the original coordinate system.

The new approach is applied to fully developed channel flow. It is found that the prescribed turbulent length scale of the synthesized turbulence has a large effect on the predicted results. As an alternative to changing the prescribed turbulent length scale, the turbulent length scale of the synthesized fluctuations can artificially be increased in the streamwise direction by changing the mapping of the fluctuations to the interface plane in the CFD domain.

Good results are obtained when the turbulent length scale is increased by a factor of four, either through the prescribed turbulent length scale or through the mapping. Very similar results are obtained when replacing the synthesized fluctuations with instantaneous DNS fluctuations (a time series). Also in this case better results are obtained when the streamwise turbulent length scale is enhanced by a factor of four by changing the mapping (i.e. the Taylor hypothesis) of the DNS fluctuations from the time domain to the interface plane.

1 Introduction

When simulating bluff body flows, LES (Large Eddy Simulations) is the ideal method. Bluff body flows are dominated by large turbulent scales which can be resolved by LES without too fine resolution and accurate results can be obtained at affordable cost [1–4]. On the other hand, doing accurate predictions of wall-bounded flows with LES is a challenging task. The near-wall grid spacing should be about one wall unit in the wall-normal direction. This is similar to the requirement in RANS (Reynolds-Averaged Navier-Stokes) using low-Re number models. The resolution requirement in wall-parallel planes for a well-resolved LES in the near-wall region expressed in wall units is approximately 100 (streamwise) and 20 (spanwise). This enables resolution of the near-wall turbulent structures in the viscous sublayer and the buffer layer consisting of high-speed in-rushes and low-speed ejections [5] (often called the streak process). At low to medium Reynolds numbers the streak process is responsible for the major part of the turbulence production. These structures must be resolved in an LES in order to get accurate results. Thus, for wall-bounded flows at high Reynolds numbers of engineering interest, the computational resource requirement of accurate LES is prohibitively large. Indeed, the requirement of near-wall grid resolution has largely deterred the introduction of LES in engineering practice.

The object of hybrid LES-RANS [6–11] is to get rid of the requirement of high near-wall resolution in wall-parallel planes. In the near-wall region (the URANS region), a low-Re number RANS turbulence model (usually an eddy-viscosity model) is used. In the outer region (the LES region), the usual LES is used, see Fig. 1. The idea is that the effect of the near-wall turbulent structures should be predicted by the RANS turbulence model rather than being resolved. The matching between the URANS region and the LES region usually takes place in the inner part of the logarithmic region (i.e. around 30 to 60 wall units away from the wall). In the LES region, coarser grid spacing in wall-parallel planes can be used. In this region the grid resolution is presumably dictated by the requirement of resolving the largest turbulent scales in the flow (which are related to the outer length scales, e.g. the boundary layer thickness), rather than the near-wall turbulent processes. The unsteady momentum equations are solved throughout the computational domain. The turbulent RANS viscosity is used in the URANS region, and the turbulent SGS viscosity is used in the LES region.

Recent work on hybrid LES-RANS can be found in [6–13]. In [6, 7, 9, 12] two-equation models were used in the URANS region and a one-equation SGS model was employed in the LES region. One-equation models were used in both regions in [10, 11]. The locations of the matching planes were determined in different ways. In some works [7, 9, 12] it was chosen along a pre-selected grid plane. In [10] it was determined by comparing the URANS and the LES turbulent length scales or it was computed from turbulence/physics requirements. Xiao *et al.* [6] used a two-equation model in the URANS region and blended it into an one-equation in the LES region. In [11] different partial differential equations for automatically finding the matching plane were investigated. In [13] a one-equation model was used in both region. The c_μ coefficient at the interface was computed dynamically to yield a smoother transition between the URANS and LES regions. Two different types of models are, either a one-equation model in both regions or a two-equation model in the URANS region coupled with a zero-equation dynamic model in the LES region.

Hybrid LES-RANS is similar to DES (Detached Eddy Simulations) [14–16]. The main difference is that the original DES aims at covering the whole attached boundary layer with URANS, whereas hybrid LES-RANS aims at covering only the inner part of the boundary layer with URANS. In later work DES has been used as a wall model [17, 18], and in this form DES is similar to hybrid LES-RANS.

Although good results have been presented with hybrid LES-RANS, it has been found that the treatment of the interface between the URANS region and the LES region is crucial for the success of method. The resolved turbulence supplied by the URANS region to the LES region does not have any reasonable turbulent characteristics and is not representative of turbulence at all. This results in too poorly resolved stresses on the LES side of the interface and this gives a hack – also referred to as

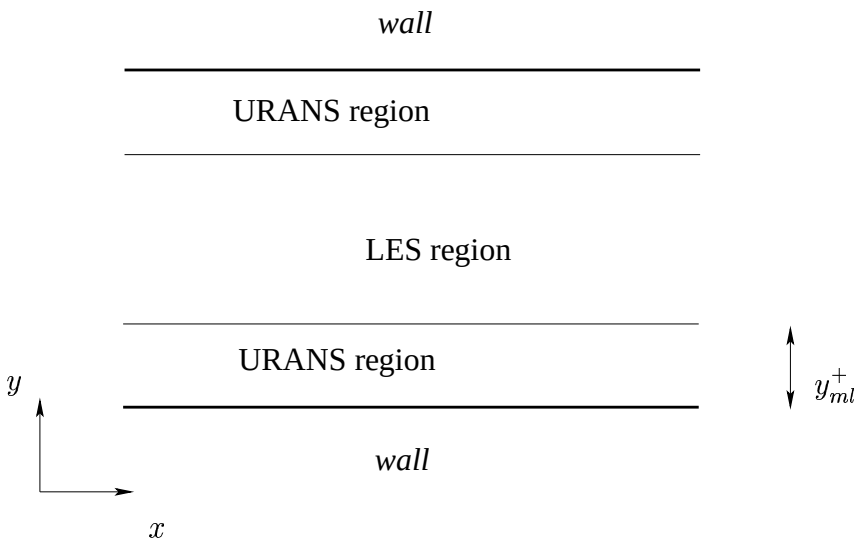

Figure 1: The LES and URANS region.

a shift – in the velocity profile approximately at the location of the matching plane [7–10, 12, 17–19]. Because the interface is located in the "constant-shear-stress-layer", the too low-resolved stresses in the LES region is via the streamwise momentum balance of the URANS region translated into too a small wall shear stress. Several modifications have been proposed to remove this deficiency. Temmermann *et al.* [8, 13] proposed to dampen the modelled stresses in the URANS region to reduce the total (i.e. resolved plus modelled) shear stress in the URANS region and thereby reducing the jump in shear stress across the matching plane. In [10] numerical smoothing was used at the interface. Hamba [12] proposed a modification of the discretized streamwise equation at the interface in order to avoid filtering out any resolved fluctuations at the interface. In [18] backscatter was introduced in the interface region with the object to generate resolved fluctuations.

In the present paper we propose to add fluctuations to the momentum equations at the LES side of the interface. The turbulent fluctuations are taken from synthesized homogeneous turbulence assuming a modified von Kármán spectrum. Both isotropic and non-isotropic fluctuations are generated. The turbulent length scale $k^{3/2}/\varepsilon$ and the turbulent kinetic energy are used as input and they are taken from time-averaged DNS data at the location of the interface plane ($y^+ = 60$). The non-isotropic fluctuations are generated in the principal coordinate system. They are then scaled to fit the DNS Reynolds tensor in the principal coordinate system. After that they are transformed back to the original coordinate system. For comparison, fluctuations are also taken from a separate DNS-simulation, an approach recently presented in [19–21].

The new approach is applied to fully developed channel flow. It is found that the prescribed turbulent length scale of the synthesized turbulence has a large effect on the predicted results. As an alternative to changing the prescribed turbulent length scale, the turbulent length scale of the synthesized fluctuations can artificially be increased by changing the mapping of the fluctuations to the interface plane in the CFD domain.

The paper is organized as follows. First the method to generate synthetic fluctuations is presented. Next, the equations and the numerical method are given. In the following section we present the DNS simulation from which the DNS fluctuations are generated. The hybrid LES-RANS method and the approach to introduce forcing fluctuations are described in the next section. After that the results are presented and discussed and conclusions are drawn in the final section.

2 Isotropic Synthesized Turbulence

A time-space turbulent velocity field can be simulated using random Fourier modes. This was proposed by Kraichnan [22] and Karweit *et al.* [23] and further developed by Bechara *et al.* [24] and Bailly and Juvé [25]. The velocity field is given by

$$u'_{i,S}(x_j) = 2\sum_{n=1}^{N} \hat{u}^n \cos(\kappa_j^n x_j + \psi^n)\sigma_i^n \tag{1}$$

where $\hat{u}^n$, ψ^n and σ_i^n are amplitude, phase and direction of the n^{th} Fourier mode, and subscript S denotes synthesized. Figure 2 shows the geometry of the n^{th} mode in wave number space.

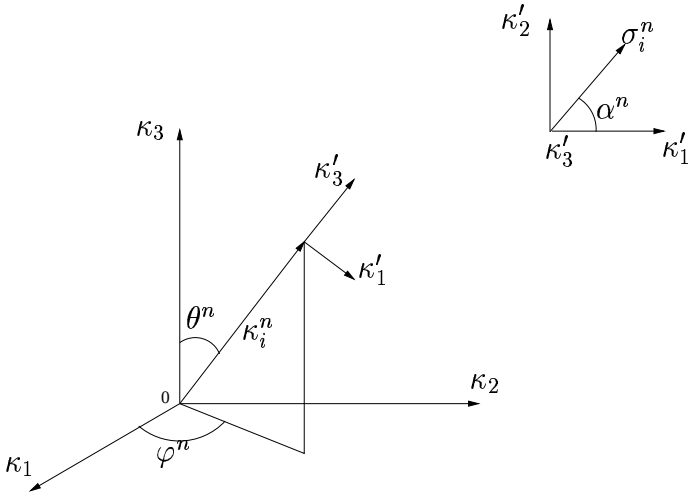

Figure 2: Geometry for the n^{th} mode.

The vector κ_i^n is chosen randomly on a sphere with radius κ^n. This to ensure isotropy of the generated velocity field. By the assumption of incompressibility the continuity equation gives the following relation

$$\kappa_i^n \sigma_i^n \equiv 0 \qquad \text{for all} \qquad n \tag{2}$$

The wave number vector κ_i^n and the spatial direction σ_i^n of the n^{th} mode are thus perpendicular. The angle α^n is a free parameter chosen randomly, see Fig. 2. The phase of each mode ψ^n is chosen with uniform probability between $0 \leq \psi^n \leq 2\pi$. The probability functions of all the random functions φ^n, ψ^n, θ^n and α^n are given in Table 1.

$p(\varphi^n) = 1/(2\pi)$	$0 \leq \varphi^n \leq 2\pi$
$p(\psi^n) = 1/(2\pi)$	$0 \leq \psi^n \leq 2\pi$
$p(\theta^n) = 1/(2)\sin(\theta)$	$0 \leq \theta^n \leq \pi$
$p(\alpha^n) = 1/(2\pi)$	$0 \leq \alpha^n \leq 2\pi$

Table 1: Probability distributions of random variables.

The probability function of θ, $p(\theta^n) = 1/2\sin(\theta)$ is chosen so that the distribution of the direction of κ_i^n is uniform on the surface of a sphere, see Fig. 3, i.e. the probability of a randomly selected direction is the same for all surface elements dA_i.

The amplitude $\hat{u}^n$ of each mode is computed so that the turbulence kinetic energy $E(\kappa^n)$ corresponds to the energy spectrum for isotropic turbulence. This gives

$$\hat{u}^n = \sqrt{E(\kappa^n)\Delta\kappa^n} \tag{3}$$

where $\Delta\kappa^n$ is a small interval in the spectrum located at κ^n, see Fig. 4. The spectrum is linearly divided into 150 intervals. A model spectrum is used to simulate the shape of an energy spectrum for isotropic turbulence. In this way the sum of the squares of $\hat{u}^n$ over all n is equal to the total turbulence kinetic energy

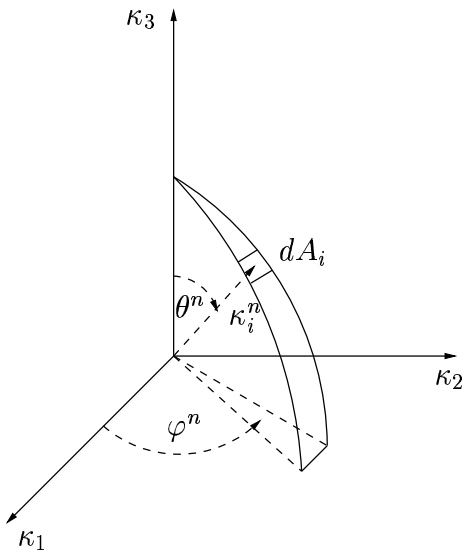

Figure 3: The probability of a randomly selected direction of a wave in wave-space is the same for all dA_i on the shell of a sphere.

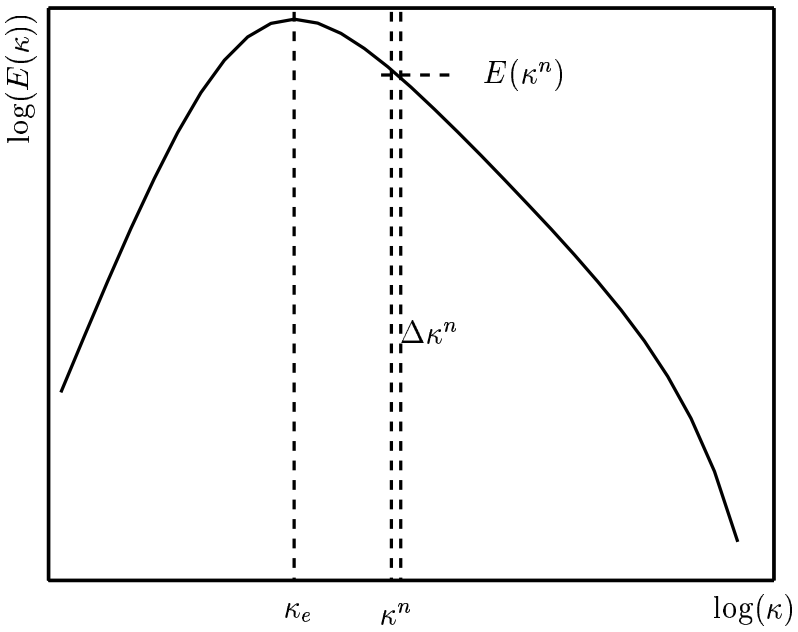

Figure 4: Modifi ed von K´arm´an spectrum

$$k = \sum_{n=1}^{N} (\hat{u}^n)^2 \tag{4}$$

The energy spectrum for isotropic turbulence is taken as a modified von Kármán spectrum

$$E(\kappa) = \alpha \frac{u_{rms}^2}{\kappa_e} \frac{(\kappa/\kappa_e)^4}{[1+(\kappa/\kappa_e)^2]^{17/6}} e^{[-2(\kappa/\kappa_\eta)^2]} \tag{5}$$

where $\kappa = (\kappa_i \kappa_i)^{1/2}$ is the wave number, $\kappa_\eta = \varepsilon^{1/4}\nu^{-3/4}$ is the Kolmogorov wave number, and κ_e corresponds to the most energetic length scales. More details can be found in [26, 27].

When generating fluctuations to be used at the interface the turbulent kinetic energy k and the integral length scale $\mathcal{L} \propto \kappa_e^{-1}$ are required as input. They are taken from the present DNS prediction at the location of the matching plane and the integral length scale is taken as $\mathcal{L} \propto k^{3/2}/\varepsilon$, see Table 3.

2.1 Non-isotropic Synthesized Turbulence

Recently an approach to use the method described above for synthesizing non-isotropic turbulent fluctuations was proposed [27, 28]. This new approach can be summarized as follows.

1. The Reynolds stress tensor and a turbulent length scale ($k^{3/2}/\varepsilon$) are supplied (in the present work taken from DNS at the location of the matching plane).

2. The principal coordinate directions of the Reynolds stress tensor are computed and the eigenvalues, i.e. the normal Reynolds stresses in the principal coordinate system, are computed.

3. The method described in the previous section is used to generate turbulent fluctuations $u^{\star\prime}_{i,S}$ in the principal coordinate system (denoted by superscript $\star$). Note that although $\langle (u^{\star\prime}_{i,S})^2 \rangle \neq \langle (u^{\star\prime}_{j,S})^2 \rangle$ $(i \neq j)$, the shear stresses in the principal coordinate system are zero.

4. The synthesized fluctuations are transformed back to the original coordinate system. In this coordinate system the Reynolds stresses of the synthesized fluctuations are equal to the supplied DNS Reynolds stress tensor (see Item 1). That means in particular that the shear stresses are non-zero (provided that that was the case for the supplied DNS Reynolds stress tensor).

3 Equations.

The Navier-Stokes equations, time-averaged (or ensemble averaged) in the near-wall regions and filtered in the core region, read

$$\frac{\partial \bar{u}_i}{\partial t} + \frac{\partial}{\partial x_j}\left(\bar{u}_i \bar{u}_j\right) = \delta_{1i} - \frac{1}{\rho}\frac{\partial \bar{p}}{\partial x_i} + \frac{\partial}{\partial x_j}\left[(\nu + \nu_T)\frac{\partial \bar{u}_i}{\partial x_j}\right] \tag{6}$$

$$\frac{\partial \bar{u}_i}{\partial x_i} = 0 \tag{7}$$

where $\nu_T = \nu_t$ (ν_t denotes the turbulent RANS viscosity) for $y \leq y_{ml}$ (see Fig. 1), otherwise $\nu_T = \nu_{sgs}$. The turbulent viscosity ν_T is computed from an algebraic turbulent length scale and k_T for which a transport equation is solved, see below. The density is set to one in all simulations.

3.1 Boundary Conditions.

No-slip conditions are used at the walls and periodic boundary conditions are used in the streamwise (x) and the spanwise direction (z). Neumann boundary conditions are used for pressure at the walls.

3.2 The Numerical Method

Second-order central differencing in space is used for all terms. An implicit, two-step time-advancement method is employed for the pressure-velocity coupling. The discrete form of Eq. 6 can be written as

$$\bar{u}_i^{n+1/2} = \bar{u}_i^n + \Delta t H\left(\bar{u}_i^n, \bar{u}_i^{n+1/2}\right) - \frac{1}{\rho}\alpha\Delta t\frac{\partial \bar{p}^{n+1/2}}{\partial x_i} - \frac{1}{\rho}(1-\alpha)\Delta t\frac{\partial \bar{p}^n}{\partial x_i} \tag{8}$$

where $H\left(\bar{u}_i^n, \bar{u}_i^{n+1/2}\right)$ includes the convection term, the viscous and the turbulent stresses, and $\alpha = 0.5$ (the Crank-Nicholson scheme). Equation 8 gives $\bar{u}_i^{n+1/2}$ which does not satisfy continuity. An intermediate velocity field is computed by subtracting the implicit part of the pressure gradient, i.e.

$$\bar{u}_i^{*} = \bar{u}_i^{n+1/2} + \frac{1}{\rho}\alpha\Delta t\frac{\partial \bar{p}^{n+1/2}}{\partial x_i}. \tag{9}$$

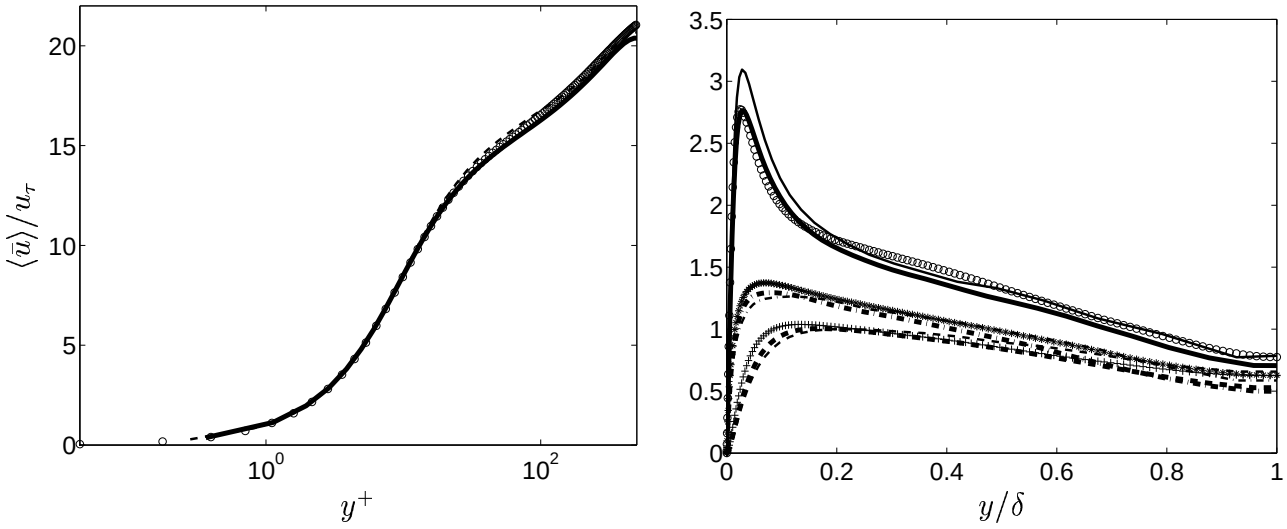

(a) Velocity profile.

(b) RMS fluctuations.

Figure 5: Streamwise $\langle \bar{u} \rangle$ profiles and resolved RMS fluctuations. Thick lines: present 96^3 DNS; thin lines: present 64^3 DNS; markers: DNS [30]

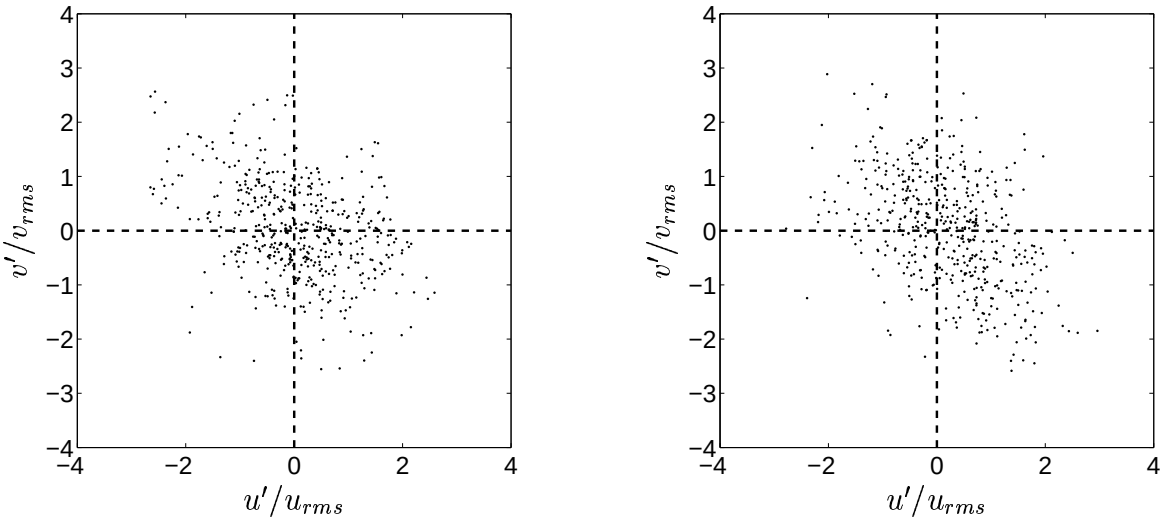

(a) Present 96^3 DNS

(b) Synthesized non-isotropic turbulence.

Figure 6: Scatter plot of u' and v' fluctuations at $y^+ = 60$.

Now $\bar{u}_i^{n+1/2}$ in Eq. 9 is replaced by the velocity field at level $(n+1)$, i.e. $\bar{u}_i^{n+1}$. Taking the divergence of Eq. 9 and requiring that the face velocities $\bar{u}_{i,f}^{n+1}$ (which are obtained by linear interpolation) satisfy the continuity equation the following Poisson equation for pressure is obtained

$$\frac{\partial^2 \bar{p}^{n+1}}{\partial x_i \partial x_i} = \frac{\rho}{\Delta t \alpha} \frac{\partial \bar{u}_{i,f}^*}{\partial x_i}. \tag{10}$$

The Poisson equation is solved with an efficient multigrid method [29]. For more details, see Ref. [7].

4 Direct Numerical Simulations.

In the present paper the fluctuations for the forcing described above are obtained from synthesized turbulence. For comparison the fluctuations are also taken from a DNS of generic boundary layer as

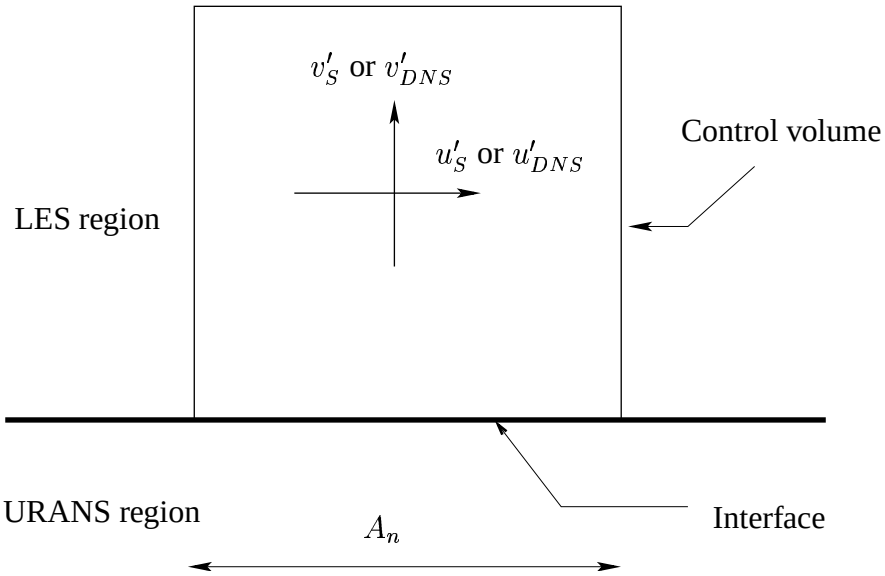

Figure 7: Added fluctuations in a control volume ($j_{ml}+1$) in the LES region adjacent to the interface. The fluctuations are either synthesized (u'_S, v'_S, w'_S) or from channel DNS (u'_{DNS}, v'_{DNS}, w'_{DNS}).

in [21]. To generate the fluctuations a DNS of channel flow at $Re_\tau = 500$ was carried out. The finite volume method presented above was used. The extent of the computational domain was $2\pi \times 2 \times 0.5\pi$ (x, y, z). Two DNS simulations have been carried out. One with $64 \times 64 \times 64$ cells and one with $96 \times 96 \times 96$ cells. The first near-wall computational node was located at $y^+ = 0.3$ for both meshes and the geometric stretching in the y direction was 17% for the 64^3 mesh and 8% for the 96^3 mesh.

The streamwise velocity profile and the resolved RMS fluctuations are in Fig. 5 compared with the DNS in [30] at $Re_\tau = 595$. As can be seen, the agreement is good.

The turbulence structure in the inner logarithmic region is only weakly dependent on Reynolds number. It is thus believed that these data can be used for forcing at the interface for a wide range of boundary layers, and that they possess realistic structural information. One aspect of this is shown in Fig. 6a in which scatter plots for quadrant analysis of the u' and v' fluctuations at $y^+ = 60$ are presented. As expected, quadrant 2 (negative u' and positive v') and quadrant 4 (positive u' and negative v') are dominating. This is also the case for the synthesized non-isotropic fluctuations, see Fig. 6b. The events corresponding to theses two quadrants contributes to negative $\langle u'v' \rangle$ correlation.

5 Hybrid LES–RANS

A one-equation model is employed in both the URANS region and LES region which reads

$$\frac{\partial k_T}{\partial t} + \frac{\partial}{\partial x_j}(\bar{u}_j k_T) = \frac{\partial}{\partial x_j}\left[(\nu + \nu_T)\frac{\partial k_T}{\partial x_j}\right] + P_{k_T} - C_\varepsilon \frac{k_T^{3/2}}{\ell} \qquad (11)$$
$$P_{k_T} = -\tau_{ij}\bar{s}_{ij}, \quad \tau_{ij} = -2\nu_T \bar{s}_{ij}$$

In the inner region ($y \leq y_{ml}$) k_T corresponds to RANS turbulent kinetic energy k; in the outer region ($y > y_{ml}$) it corresponds to subgrid-scale kinetic turbulent energy (k_{sgs}). No special treatment is used in the equations at the matching plane except that the form of the turbulent viscosity and the turbulent length scale are different in the two regions, see Table 2. At walls $k_T = 0$.

5.1 Forcing conditions

In this section we present how forcing conditions are implemented and how the synthesized fluctuations and DNS fluctuations are mapped to the CFD domain.

The synthesized or DNS fluctuations are added as momentum sources in the cells in the LES region

	URANS region	LES region
ℓ	$2.5n[1-\exp(-0.2k^{1/2}n/\nu)]$	$\ell=\Delta=(\delta V)^{1/3}$
ν_T	$2.5k^{1/2}n[1-\exp(-0.014k^{1/2}n/\nu)]$	$0.07k^{1/2}\ell$
C_ε	1.0	1.07

Table 2: Turbulent viscosities and turbulent length scales in the URANS and LES regions. n denotes the distance to the nearest wall.

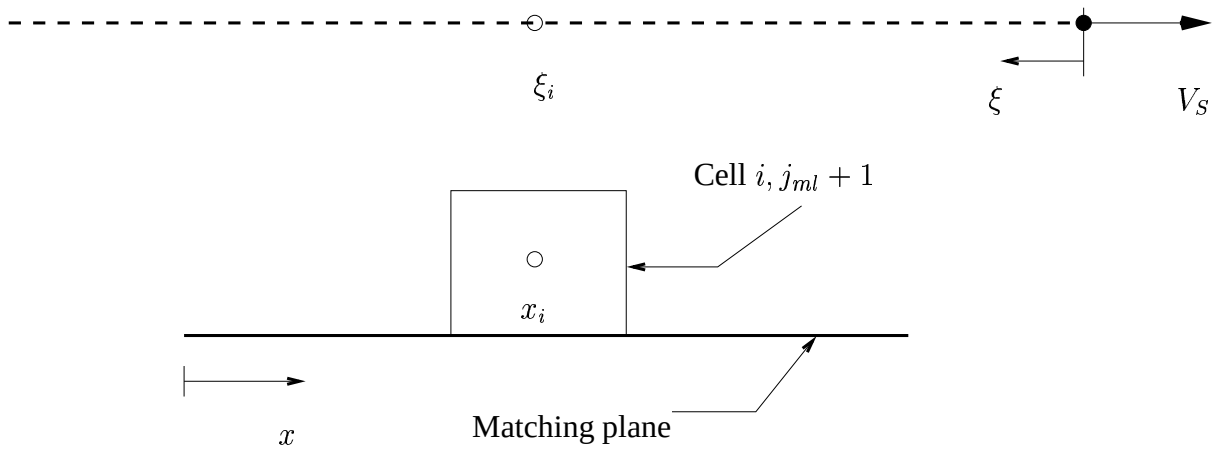

Figure 8: Mapping of synthesized fluctuations from the $\xi-\zeta$ plane (dashed line) to the computational $x-z$ plane at $y=y_{ml}$, see Eq. 14. $\Delta x=10\Delta\xi$. The $\xi-\zeta$ plane is moving to the right with speed $V_S=\langle\bar{u}_{j_{ml}+1}\rangle$

adjacent to the matching plane, see Fig. 7. The sources for the three momentum equations read

$$S_U=-\gamma\rho u_f'v_f'A_n,\quad S_V=-\gamma\rho v_f'v_f'A_n,\quad S_W=-\gamma\rho w_f'v_f'A_n \tag{12}$$

(index f is either DNS or S) where A_n is the area of the control volume, and $\gamma=c_\gamma k_T(x,y_{ml},z)/k_{fluct}$, where k_{fluct} is the turbulent kinetic energy of the DNS fluctuations or the synthesized fluctuations. In the former case $c_\gamma=0.4$, whereas in the latter case $c_\gamma=1$. It should be noted that the time-averaged momentum forces are non-zero if there is a correlation between the added fluctuating velocity components. For DNS and non-isotropic fluctuations the momentum source in the $\bar{u}$ equation is thus positive since $-\langle u_f'v_f'\rangle>0$. This gives a friction velocity $u_{*,w}>1$ (see Table 3) since the wall shear stresses must now balance both the driving pressure gradient as well as the added momentum source $\langle S_U\rangle$ [21]. For isotropic fluctuations $\langle u_S'v_S'\rangle=0$ and thus $u_{*,w}=1$

5.2 Mapping of forcing fluctuations to the CFD domain

Synthesized turbulence is generated as a single realization in a large two-dimensional $\xi-\zeta$ plane which extends $z_{max}/2$ (16 cells of size Δz) in the z direction and $5000\Delta x$ (50 000 cells of size $0.1\Delta x$) in the x direction. Periodic conditions are assumed in the z direction to cover the entire width of the CFD domain. In order to map synthesized turbulence at each time step and streamwise position to the CFD computational domain, it is imagined that the $\xi-\zeta$ plane is convected at a constant speed V_S in the x direction, see Fig. 8. V_S is taken as the time-averaged velocity at the location of the matching plane, i.e. $V_S=\langle\bar{u}\rangle_{y_{ml}}$. In this way the u_S' fluctuation, for example, is mapped from the $\xi-\zeta$ plane to the $x-z$ CFD plane as

$$u_S'(x,y_{ml},z,t)=u_S'(\xi,\zeta),\quad \xi=V_St+x_{max}-x,\quad \zeta=\min(z,z-0.5z_{max}) \tag{13}$$

The mapping in discrete form reads

$$\xi_i=10M_S(V_St+x_{max}-x_i)/\Delta x \tag{14}$$

(the factor 10 appears because $\Delta x/\Delta\xi=10$). Different values of M_S have been used, see Table 3. A low M_S value gives an increased streamwise turbulent length scale.

Forcing	$\mathcal{L}$	M_{DNS}	M_S	$u_{*,w}$
none	-	-	-	1
DNS	-	1	-	1.15
DNS	-	0.25	-	1.15
Isotropic	$k^{3/2}/\varepsilon$	-	1	1
Isotropic	$k^{3/2}/\varepsilon$	-	0.25	1
Non-isotropic	$k^{3/2}/\varepsilon$	-	1	1.2
Non-isotropic	$4k^{3/2}/\varepsilon$	-	1	1.2
Non-isotropic	$k^{3/2}/\varepsilon$	-	0.25	1.2

Table 3: Presentation of test cases. Type of forcing used; integral length scale used when generating synthetic fluctuations; values of M_S and M_{DNS} used for mapping (see Eqs. 14 and 15); the predicted friction velocity.

The DNS fluctuations are generated as a time series at $x = x_0$ along the z direction from the present 64^3 simulations. The Taylor hypothesis is used to map DNS fluctuations from the time domain (τ) to the matching plane at each instant [21]. For the streamwise fluctuation, for example, we get

$$u'_{DNS}(x, y_{ml}, z, t) = u'_{DNS}\left(x_0, y_{ml}, z, \tau\right), \quad \tau = M_{DNS}(t - (x - x_0)/V_S), \quad V_S = \langle \bar{u}_{y_{ml}} \rangle \tag{15}$$

For more details, see [21] (note that in [21] $M_{DNS} = 0.25$ was used).

6 Results

Fully developed channel flow at $Re_\tau = u_\tau \delta/\nu = 2000$ (δ denotes channel half width) is used as a test case to evaluate the effect of different forcing conditions. This flow may seem as an easy test case. This is not true. When trying to improve the performance of LES in wall-bounded flows, the Achilles' heel is the near-wall flow region. The bulk velocity in fully developed channel flow with periodic boundary conditions (see Eq. 6) is entirely determined by the wall shear stress and consequently the flow is extremely sensitive to the turbulence in the near-wall region. An incorrectly predicted wall shear stress gives an incorrect bulk flow.

A coarse mesh has on purpose been chosen. The mesh has 32 cells both in streamwise (x) and spanwise (z) direction. The size of the computational domain is $x_{max} = 4\pi$, $y_{max} = 2$ (geometric stretching of 14%) and $z_{max} = 2\pi$. This gives a Δx^+ and Δz^+ of approximately 785 and 393, respectively. The location of the matching plane is $y = 0.031$ (lower wall) which corresponds to $y^+ = 62$ and 11 cells ($= j_{ml} - 1$) are used in the URANS region at each wall. A larger computational domain is used compared to in [21] because one of the cases (non-isotropic forcing with $\mathcal{L}$ and $M_S = 1$) gave steady flow with $z_{max} = \pi$. Care has been taken to ensure that all results presented are independent of the size of the computational domain.

6.1 The influence of forcing conditions.

In [19–21] forcing conditions employing DNS fluctuations were used to improve the performance of LES of wall-bounded flows at high Reynolds number. The main argument for introducing forcing conditions is that the LES region at the interface plane is supplied with poor boundary conditions from the URANS region. Although the flow coming from the URANS region indeed is unsteady (it is triggered by the LES region) it does not have any proper resolved turbulent structures. The length scales and time scales of the unsteadiness in the URANS region are not related to large-scale turbulence at all because a large part of the turbulence in the URANS region is modelled. An example of this can be seen in Fig. 9a where two-point correlations of $u'u'$ are shown for hybrid LES-RANS with and without forcing conditions and they are compared with DNS data. Here we find that the two-point correlation for hybrid LES-RANS without forcing conditions is very large indeed. This is a good illustration of the lack of proper turbulent structures in the URANS region (the two-point

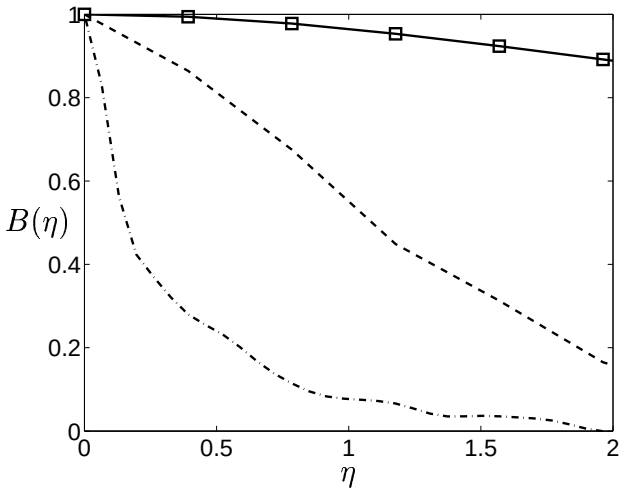

(a) $B(\eta) = \langle u'(x)u'(x+\eta)\rangle / u^2_{rms}$ at $y^+ = 60$ (in the LES region adjacent to the interface plane).

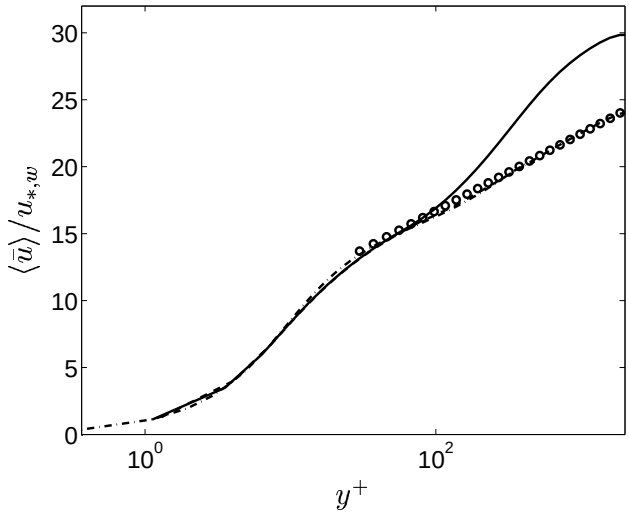

(b) $\langle \bar{u} \rangle$ profiles. $\circ$: $0.4\ln(y^+) + 5.2$

Figure 9: Two-point correlations and mean velocities. Solid lines: no forcing; dashed lines: forcing with DNS fluctuations with $M_{DNS} = 0.25$; dash-dotted lines: present 96^3 DNS.

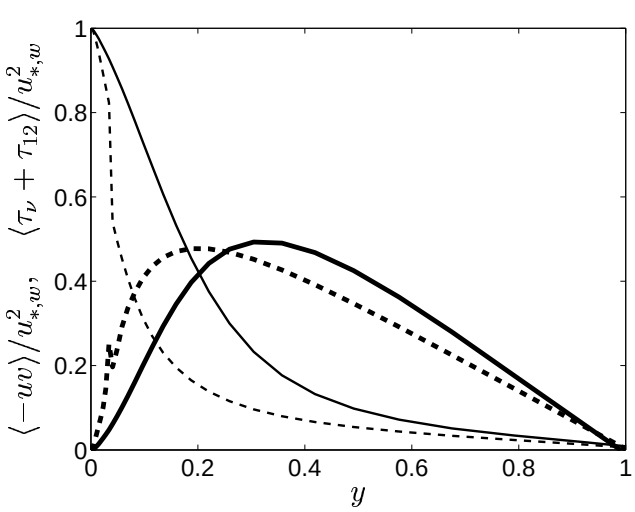

(a) Shear stresses. τ_ν denotes viscous stress.

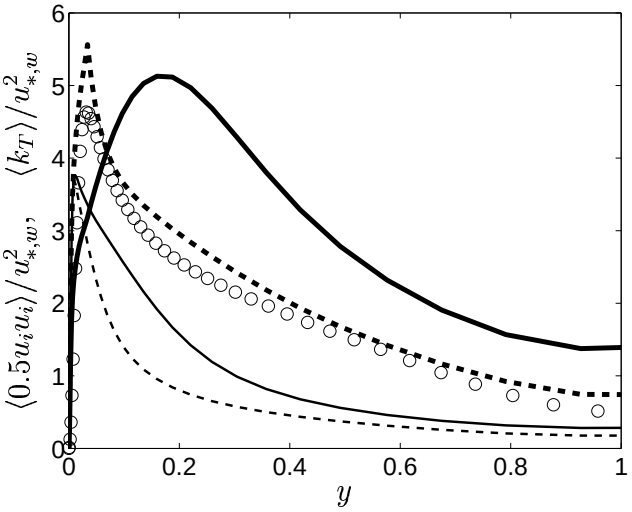

(b) Turbulent kinetic energy.

Figure 10: Shear stress and turbulent kinetic energy. Solid lines: no forcing; dashed lines: forcing with DNS fluctuations with $M_{DNS} = 0.25$. Thick lines: resolved; thin lines: modelled.

correlation is almost constant in the entire URANS region [not shown]). When forcing conditions are added the two-point correlation is drastically reduced, although is does not attain the low values of the DNS data. Considering the coarse resolution (indicated in Fig. 9a by squares) this should probably not be expected.

The streamwise velocity profiles obtained with and without forcing are compared in Fig. 9b with present DNS and the log-law. It can be seen that the centerline velocity is strongly over-predicted when no forcing is used. This is because the shear stress (or rather the wall-normal derivative of it) is too small when no forcing is used. The shear stresses are presented in Fig. 10a, and from this figure it is not obvious at all that the shear stress obtained with no forcing is too small. Indeed, it seems to be vice versa. The reason is that our periodic channel flow simulations are driven by a

constant pressure gradient (the first term on the right-hand side of Eq. 6). Averaging the equation for the streamwise component in the homogeneous directions (i.e. x, z and time) and integrating the resulting one-dimensional Reynolds equation from $y = 0$ to y we get

$$0 = \underbrace{y - \langle uv \rangle\Big|_y + (\nu + \nu_T)\frac{\partial \bar{u}}{\partial y}\Big|_y}_{\tau_{tot}} - 1 \tag{16}$$

where the terms represent the prescribed driving pressure gradient, the resolved turbulent shear stress at y, the viscous and modelled turbulent shear stress at y, and the wall shear stress, respectively. We get the usual result that the total stress must behave as

$$\tau_{tot} = 1 - y \tag{17}$$

irrespectively of turbulence model or forcing condition used. The way the momentum equations adapt to satisfy linear variation in τ_{tot} (Eq. 17) is by increasing the velocity gradient, whose effect is to increase all three types of shear stresses, both the viscous, the modelled and the resolved ones.

From Fig. 10a it is seen that the modelled shear stress for the non-forcing case is much larger than for the forcing case. The reason is that in order to satisfy Eq. 17 the velocity gradient is increased and thereby also ν_T due to increase in P_k and k_T and the increased turbulent viscosity increases the modelled shear stress. The resolved shear stress for the non-forcing case is reduced for $y \lesssim 0.2$ compared to the forcing case partly because of the large modelled shear stress (Eq. 17 must be satisfied) and partly because of the increased SGS/URANS dissipation due to large ν_T.

The relation between resolved and modelled turbulent kinetic energy, see Fig. 10b, follows that of the shear stresses. Although the equation system Eqs. 6 and 11 is strongly non-linear and coupled, which implies a mutual coupling of k_T and the shear stress, the shear stresses are governed by Eq. 17 and consequently they have a larger influence on the turbulent kinetic energies than vice versa. It can be seen that the total turbulent kinetic energy (i.e. resolved plus modelled) is strongly over-predicted both with and without forcing. This has been observed in many hybrid LES-RANS investigations [8, 10, 21]. The over-predicted turbulent kinetic energy is closely connected to the fact that the equation system must satisfy the momentum equation, i.e. Eq. 16 which determines the resolved stresses and the mean strain rate. This in turn gives a certain production of both modelled and resolved turbulent kinetic energy, which turn out to be too large and which indicates that we need to modify our RANS turbulence models. These models were, after all, developed and tuned for steady flow, not for flows in which a significant amount of the turbulence is resolved. Some modifications have been proposed in which the modelled part of the turbulence was reduced by reducing the C_μ coefficient [13].

6.2 Forcing conditions from synthesized turbulence.

In Fig. 11 the streamwise velocity and the turbulent kinetic energy are presented for isotropic and non-isotropic forcing conditions. In both cases the velocity profile is slightly over-predicted. As in the case of forcing with DNS fluctuations (Fig. 10b), the total turbulent kinetic energy is as expected over-predicted. However, the resolved turbulent kinetic energy predicted with non-isotropic forcing agrees fairly well the DNS data whereas it is strongly over-predicted with isotropic forcing. The source to the large difference in resolved turbulent kinetic energy is found in Fig. 12. The resolved shear stress $-\langle uv \rangle$ is much larger with isotropic forcing than with non-isotropic forcing. In Fig. 12b a zoomed view of the shear stresses is shown. Here, for the non-isotropic forcing the large jump in the modelled shear stress at the location of the matching plane is clearly seen. It should be mentioned that this jump is not related to the streamwise periodic boundary conditions with a driving pressure gradient; it also appears when inlet-outlet boundary conditions are used [21]. The jump corresponds to the averaged added momentum force $\langle S_U \rangle$ (see Eq. 12). The global momentum balance requires that $u^2_{*,w} - 1 = \langle S_U \rangle$ [21] which is equal to 0.44, see Table 3. Note that in Fig. 12 the jump is equal

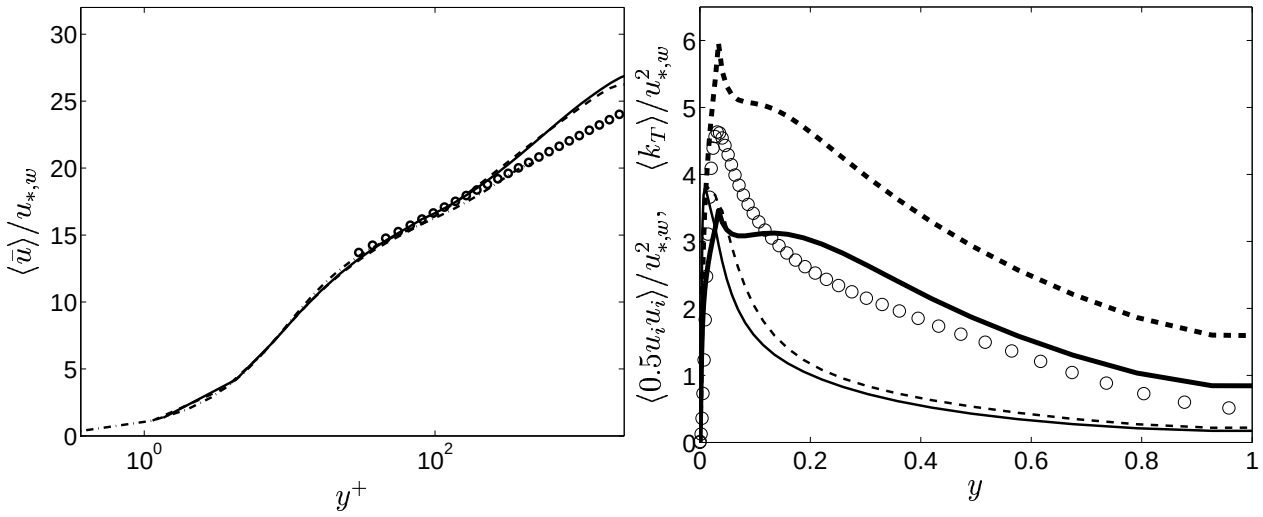

(a) $\langle \bar{u} \rangle$ profiles. $\circ$: $0.4 \ln(y^+) + 5.2$; dash-dotted line: DNS.

(b) Turbulent kinetic energy. Thick lines: resolved; thin lines: modelled; $\circ$: k_{DNS}.

Figure 11: Streamwise velocities and turbulent kinetic energy. $M_S = 1$. Solid lines: forcing with non-isotropic fluctuations; dashed lines: forcing with isotropic fluctuations. DNS data from present 96^3 DNS.

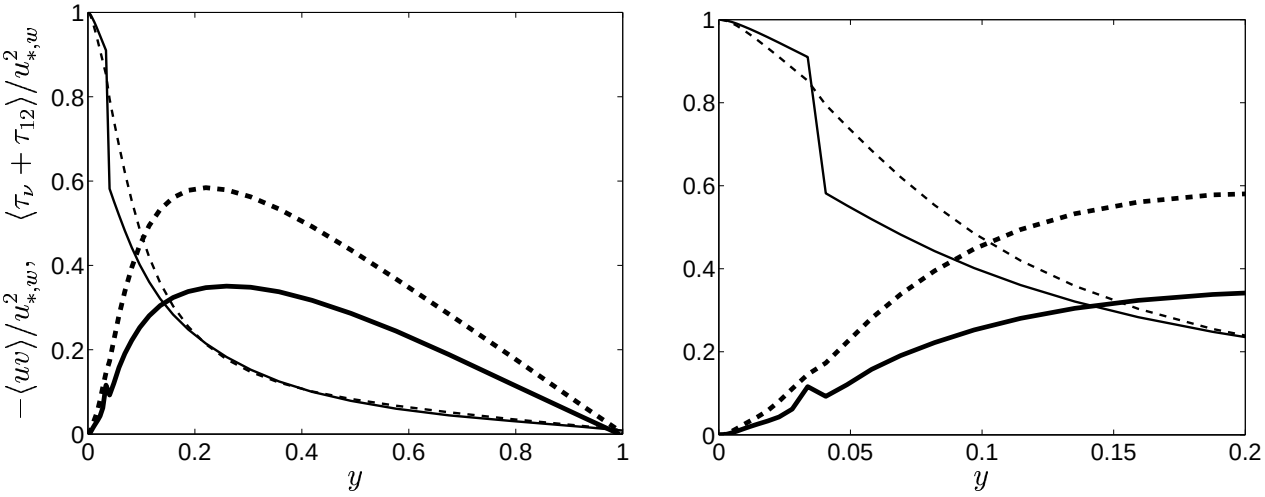

(a) Full view

(b) Zoomed view.

Figure 12: Shear stresses. $M_S = 1$. τ_ν denotes viscous shear stress. Solid lines: forcing with non-isotropic fluctuations; dashed lines: forcing with isotropic fluctuations. Thick lines: resolved; thin lines: modelled.

to $0.44/1.44$ since all terms in Fig. 12 are scaled with $u^2_{*,w}$. The added momentum must be taken up by the wall shear stress in order to satisfy global momentum balance. As can be seen from Eq. 12b the modelled and viscous diffusion transports the additional momentum from the interface plane to the wall (at the interface, i.e. $y = 0.03$, the ratio between the modelled and physical viscosity is $\nu_T/\nu = 20$ and the ratio decreases towards the wall; at $y = 0.005$ the ratio is approximately one). As a consequence of the added momentum source, the total shear stress at the LES side of the interface plane for the non-isotropic case is smaller than for the isotropic case, the difference being equal to $\langle S_U \rangle$. This explains why the resolved stress is much smaller in the non-isotropic forcing case than in the isotropic forcing case, see Fig. 12. It also illustrates the fact that it is not the time-averaged momentum source that is important (it is indeed zero for the isotropic fluctuations), but it is the

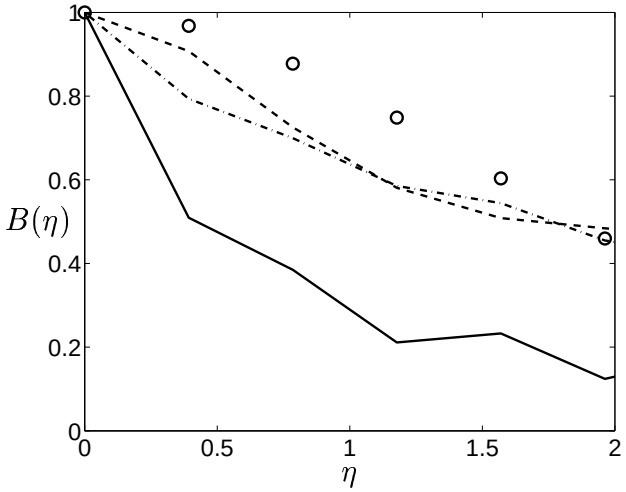

(a) Forcing with non-isotropic fluctuations. Solid lines: $M_S = 1$; dashed lines: $M_S = 0.25$; dash-dotted: $4\mathcal{L}$.

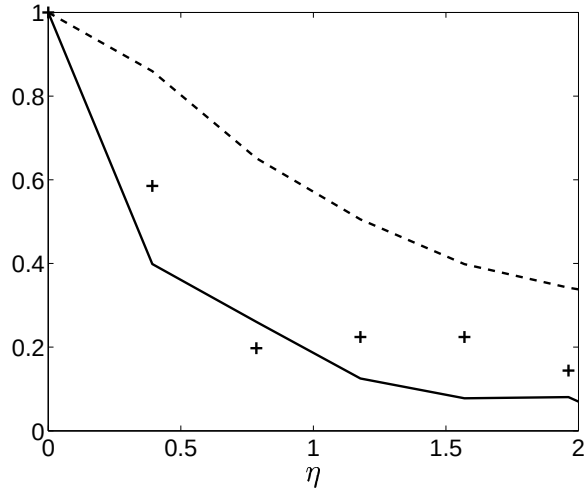

(b) Forcing with isotropic fluctuations. Solid lines: $M_S = 1$; dashed lines: $M_S = 0.25$.

Figure 13: Two-point correlations $B(\eta) = \langle u'(x)u'(x+\eta)\rangle / u_{rms}^2$ of the added fluctuations. $\circ$: DNS fluctuations using $M_{DNS} = 0.25$; $+$: DNS fluctuations using $M_{DNS} = 1$.

Forcing	$\mathcal{L}$	M_{DNS}	M_S	$\mathcal{L}_x$	$\mathcal{L}_z$
isotropic	0.35	-	1	0.55	0.22
isotropic	0.35	-	0.25	1.94	0.18
non-isotropic	0.35	-	1	0.68	0.18
non-isotropic	0.35	-	0.25	2.50	0.17
non-isotropic	1.4	-	1	2.16	0.5
DNS	-	1	-	0.54	0.28
DNS	-	0.25	-	2.05	0.21

Table 4: Integral length scales of forcing fluctuations. $\mathcal{L}$ denotes integral length scale used when synthesizing fluctuations; $\mathcal{L}_x$ and $\mathcal{L}_z$ denote integral length scales computed from the DNS or synthesized fluctuations.

turbulent structures which are crucial. If a constant momentum source is added at the interface plane, the predicted velocity profile does not improve, but all that happens is that the wall shear stress is increased by the same magnitude.

Comparing the velocity profiles obtained with DNS fluctuations and non-isotropic fluctuations Figs. 9b and 11a the profiles are better predicted in the former case. One important difference between the imposed fluctuations is that the streamwise length scale of the added DNS fluctuations has been artificially enhanced by using $M_{DNS} = 0.25$, see Eq. 15. This gives an increase in $\mathcal{L}_x$ of approximately four, see Table 4 and Fig. 9a. Thus, the integral length scales of the synthetic fluctuations were also enhanced by reducing M_S to $M_S = 0.25$ in Eq. 14. The resulting two-point correlations and integral length scales $\mathcal{L}_x$ are shown in Fig. 13 and Table 4. It can be seen that decreasing M_S for the synthetic fluctuations gives a similar effect as for the DNS fluctuations. It is reasonable to artificially enhance the streamwise length scale considering that the streamwise resolution in the simulations is similar to original streamwise integral length scale ($\Delta x \simeq 0.4$ and $\mathcal{L}_x \simeq 0.5$ ($M_S = 1$)). It does not make sense to add fluctuations (DNS or synthetic) whose integral length scales are smaller than the grid resolution. The same argument can indeed be made for the spanwise direction for which the situation is similar: the integral length scale is $\mathcal{L}_z \simeq 0.2$ and the resolution is $\Delta z \simeq 0.2$. No tests have been carried out with enhanced integral spanwise length scales.

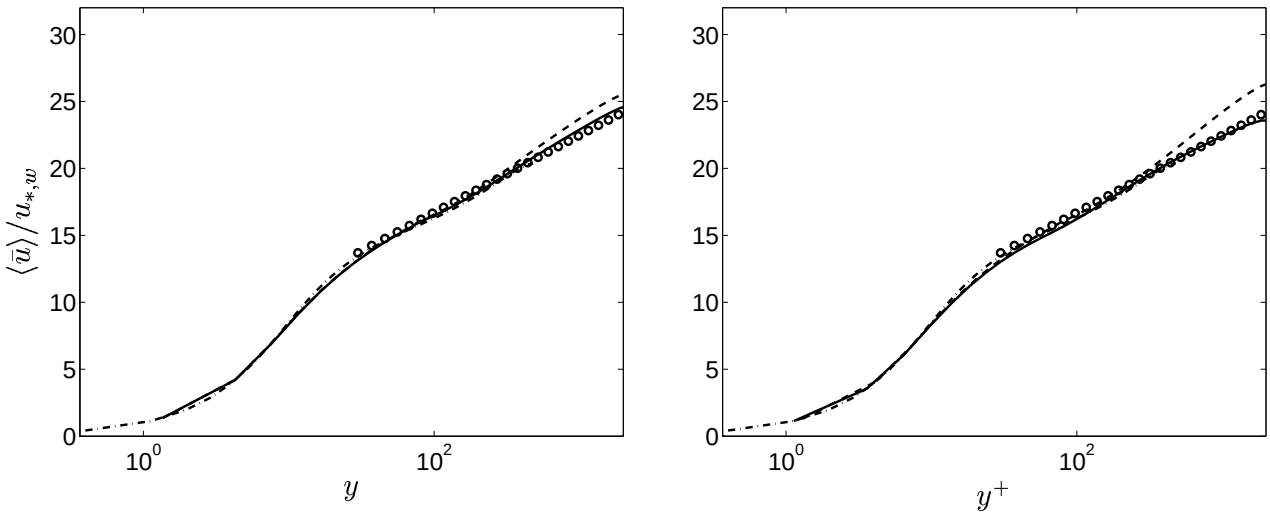

(a) Solid line: non-isotropic forcing with $M_S = 0.25$; dashed line: non-isotropic forcing with $4\mathcal{L}$.

(b) Solid line: isotropic forcing with $M_S = 0.25$; dashed line: DNS forcing with $M_{DNS} = 1$.

Figure 14: Streamwise velocities. $\langle\bar{u}\rangle$ profi les. $\circ$: $0.4\ln(y^+) + 5.2$; dash-dotted line: present 96^3 DNS.

The spanwise integral length scales $\mathcal{L}_z$ are also included in Table 4. For isotropic fluctuations it is much smaller than $\mathcal{L}_x$ although they should be equal. The reason is probably the coarse resolution which makes evaluation of $\mathcal{L}_z$ inexact. It can be noted that for the non-isotropic fluctuations the ratio between the streamwise and spanwise integral length scale is even larger. This is expected since in order to satisfy continuity the length scales of the synthesized non-isotropic fluctuations are re-scaled making the turbulent length scales larger in the principal direction of the largest fluctuations and vice versa [27, 28].

When synthesizing fluctuations we can enhance the turbulent length scale by increasing the integral length scale $\mathcal{L}$ used as input. Whereas an decrease in M_S only increases the streamwise length scale, an increase of $\mathcal{L}$ increases the turbulent length scale in both streamwise and spanwise direction. As mentioned above this may or may not be a disadvantage. Tests have been carried out where $\mathcal{L}$ has been increased by a factor of four when generating non-isotropic synthetic fluctuations, see Table 3. The resulting two-point correlation and integral length scales are shown in Fig. 13 and Table 4. It can be seen that increasing $\mathcal{L}$ by a factor of four gives a similar effect as decreasing M_S by a factor of four. One difference is that in the former case the spanwise length scale is also increased. This may or may not be an effect that we wish. On one hand, the spanwise integral length scale of the synthesized fluctuations becomes approximately twice as large as indicated by the DNS data. On the other hand, since the spanwise scales are larger, they are more suitable for the spanwise grid resolution.

In Fig. 14 the velocity profiles using isotropic and non-isotropic fluctuations with an increased turbulent length scale are presented. It can be seen that for both non-isotropic forcing (Fig. 14a) and isotropic forcing (Fig. 14b) slightly better results are obtained when the streamwise length scale is increased by setting $M_S = 0.25$ than by prescribing a four times larger length scale when generating the fluctuations. The velocity profiles obtained with forcing from DNS fluctuations are also included in Fig. 14b, and it is seen that the artificial enhancement of the streamwise turbulent length scale ($M_{DNS} = 0.25$) improves the results (cf. Fig. 9b).

Figure 15 compares predicted shear stresses obtained with $M_S = 1$ and $M_S = 0.25$. For both isotropic and non-isotropic forcing it can be seen that reducing M_S from 1 to 0.25 increases the resolved shear stress and decreases the modelled one, without affecting the total shear stress which obeys Eq. 17. Here it is again illustrated that the reason when we in hybrid LES-RANS get too large velocities (or rather too large U_b/u_*) it is not due to too large *modelled* shear stresses but because of too small *resolved* shear stresses. When decreasing M_S from 1 to 0.25, thereby increasing the

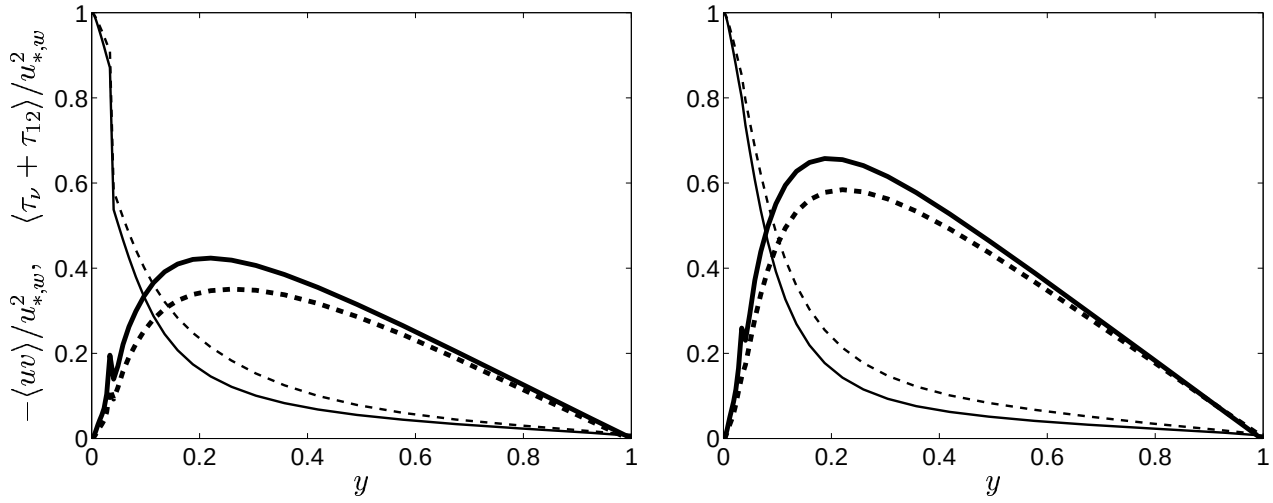

(a) Non-isotropic forcing.

(b) Isotropic forcing.

Figure 15: Shear stresses. Solid line: $M_S = 0.25$; dashed line: $M = 1$. Thick lines: resolved; thin lines: modelled.

streamwise turbulent length scale by approximately a factor of four, the resolved shear stresses are increased (Fig. 15) which increases the diffusion of streamwise momentum. The result is a lower velocity in the center region of the channel, cf. Figs. 11 and 14.

7 Conclusions

Hybrid LES-RANS predictions of channel flow have been presented. It is argued that the main reason why standard LES-RANS performs rather poorly is that the LES region at the interface is supplied with incorrect turbulent structures from the URANS region and as a result the resolved turbulent shear stress in the LES region becomes too small. To improve the performance of the model turbulent fluctuations are added at the interface. The turbulent fluctuations are generated by assuming they obey a modified von Kármán spectrum. A turbulent length and velocity scale, taken from DNS channel flow data at the location of the matching plane, are used as input data when generating (synthesizing) the fluctuations. The obtained results are considerably improved, but still disagrees with the log-law with typically 13%. It is found that by increasing the streamwise turbulent length scale of the added turbulent fluctuations by a factor of four, good results are obtained.

7.1 Acknowledgments.

This work was financed by the FLOMANIA project (Flow Physics Modelling – An Integrated Approach) and is a collaboration between Alenia, AEA, Bombardier, Dassault, EADS-CASA, EADS-Military Aircraft, EDF, NUMECA, DLR, FOI, IMFT, ONERA, Chalmers University, Imperial College, TU Berlin, UMIST and St. Petersburg State University. The project is funded by the European Union and administrated by the CEC, Research Directorate-General, Growth Programme, under Contract No. G4RD-CT2001-00613.

REFERENCES

[1] W. Rodi, J.H. Ferziger, M. Breuer, and M. Pourquié. Status of large-eddy simulations: Results of a workshop. *J. Fluids Engineering*, pages 248–262, 1997.

[2] S. Krajnović and L. Davidson. Large eddy simulation of the flow around an Ahmed body. In *2004 ASME Heat Transfer/Fluids Engineering Summer Conference*, Charlotte, North Carolina, USA, 2004.

[3] S. Krajnović and L. Davidson. Numerical study of the flow around the bus-shaped body. *ASME: Journal of Fluids Engineering*, 125:500–509, 2003.

[4] S. Krajnović and L. Davidson. Large eddy simulation of the flow around a bluff body. *AIAA Journal*, 40(5):927–936, 2002.

[5] S.R. Robinson. Coherent motions in the turbulent boundary layer. *Annual Review of Fluid Mechanics*, 23:601–639, 1991.

[6] X. Xiao, J.R. Edwards, and H.A. Hassan. Inflow boundary conditions for LES/RANS simulations with applications to shock wave boundary layer interactions. AIAA paper 2003–0079, Reno, NV, 2003.

[7] L. Davidson and S.-H. Peng. Hybrid LES-RANS: A one-equation SGS model combined with a $k-\omega$ model for predicting recirculating flows. *International Journal for Numerical Methods in Fluids*, 43:1003–1018, 2003.

[8] L. Temmermann, M.A. Leschziner, and K. Hanjalić. A-priori studies of near-wall RANS model within a hybrid LES/RANS scheme. In W. Rodi and N. Fueyo, editors, *Engineering Turbulence Modelling and Experiments 5*, pages 317–326. Elsevier, 2002.

[9] L. Davidson. Hybrid LES-RANS: A combination of a one-equation SGS model and a $k-\omega$ model for predicting recirculating flows. In *ECCOMAS CFD Conference*, Swansea, U.K., 2001.

[10] P. Tucker and L. Davidson. Zonal k-l based large eddy simulation. *Computers & Fluids*, 33(2):267–287, 2004.

[11] P. Tucker. Differential equation based length scales to improve DES and RANS simulations. AIAA paper 2003-3968, 16th AIAA CFD Conference, 2003.

[12] F. Hamba. An approach to hybrid RANS/LES calculation of channel flow. In W. Rodi and N. Fueyo, editors, *Engineering Turbulence Modelling and Experiments 5*, pages 297–305. Elsevier, 2003.

[13] L. Temmerman, M. Hadžiadbic, M.A. Leschziner, and K. Hanjalić. A hybrid two-layer URANS-LES approach for large eddy simulation at high Reynolds numbers (submitted). *International Journal of Heat and Fluid Flow*, 2004.

[14] P.R. Spalart, W.-H. Jou, M. Strelets, and S.R. Allmaras. Comments on the feasability of LES for wings and on a hybrid RANS/LES approach. In C. Liu and Z. Liu, editors, *Advances in LES/DNS, First Int. conf. on DNS/LES*, Louisiana Tech University, 1997. Greyden Press.

[15] P.R. Spalart. Strategies for turbulence modelling and simulations. *International Journal of Heat and Fluid Flow*, 21:252–263, 2000.

[16] M. Strelets. Detached eddy simulation of massively separated flows. AIAA paper 2001–0879, Reno, NV, 2001.

[17] N.V. Nikiton, F. Nicoud, B. Wasistho, K.D. Squires, and P. Spalart. An approach to wall modeling in large-eddy simulations. *Physics of Fluids A*, 12(7):1629–1632, 2000.

[18] U. Piomelli, E. Balaras, H. Pasinato, K.D. Squire, and P.R. Spalart. The inner-outer layer interface in large-eddy simulations with wall-layer models. *International Journal of Heat and Fluid Flow*, 24:538–550, 2003.

[19] S. Dahlstr¨om. *Large Eddy Simulation of the Flow Around a High-Lift Airfoil*. PhD thesis, Dept. of Thermo and Fluid Dynamics, Chalmers University of Technology, G¨oteborg, Sweden, 2003.

[20] S. Dahlstr¨om and L. Davidson. Hybrid RANS-LES with additional conditions at the matching region. In K. Hanjalić, Y. Nagano, and M.J. Tummers, editors, *Turbulence Heat and Mass Transfer 4*, pages 689–696, New York, Wallingford (UK), 2003. begell house, inc.

[21] L. Davidson and S. Dahlstr¨om. Hybrid RANS-LES an approach to make LES applicable at high Reynolds number. In *International Symposium on Advanced in Computational Heat Transfer*, April 19-24, Norway (Keynote Lecture), 2004.

[22] R.H. Kraichnan. Diffusion by a random velocity field. *Journal of Computational Physics*, 13(1):22–31, 1970.

[23] M. Karweit, P. Blanc-Benon, D. Juvé, and G. Comte-Bellot. Simulation of the propagation of an acoustic wave through a turbulent velocity field: A study of phase variance. *J. Acoust. Soc. Am*, 89(1):52–62, 1991.

[24] W. Bechara, C. Bailly, and P. Lafon. Stochastic approach to noise modeling for free turbulent flows. *AIAA Journal*, 32 , No. 3:455–463, 1994.

[25] C. Bailly and D. Juvé. A stochastic approach to compute subsonic noise using linearized Euler's equations. *AIAA Journal*, 99-1872, 1999.

[26] M. Billson, L.-E. Eriksson, and L. Davidson. Jet noise prediction using stochastic turbulence modeling. AIAA paper 2003-3282, 9th AIAA/CEAS Aeroacoustics Conference, 2003.

[27] M. Billson. *Computational Techniques for Turbulence Generated Noise*. PhD thesis, Dept. of Thermo and Fluid Dynamics, Chalmers University of Technology, G¨oteborg, Sweden, 2004.

[28] M. Billson, L.-E. Eriksson, and L. Davidson. Modeling of synthetic anisotropic turbulence and its sound emission. The 10th AIAA/CEAS Aeroacoustics Conference, AIAA 2004-2857, Manchester, United Kindom, 2004, 2004.

[29] P. Emvin. *The Full Multigrid Method Applied to Turbulent Flow in Ventilated Enclosures Using Structured and Unstructured Grids*. PhD thesis, Dept. of Thermo and Fluid Dynamics, Chalmers University of Technology, G¨oteborg, 1997.

[30] R.D. Moser, J.D. Kim, and N.N. Mansour. Direct numerical simulation of turbulent channel flow up to $Re_\tau = 590$. *Physics of Fluids A*, 11:943–945, 1999.